PHYSICAL REVIEW APPLIED **20,** 024075 (2023)

Tuning Layer-, Perfect-Spin-, and Valley-Polarized Transport in Transition-Metal-Dichalcogenide Bilayer Junctions

Yaser Hajati,[1,2,*] Mohammad Alipourzadeh,[2] Dominik Schulz,[1] and Jamal Berakdar[1]

[1] *Institut für Physik, Martin-Luther Universität Halle-Wittenberg, 06099 Halle, Germany*

[2] *Department of Physics, Faculty of Science, Shahid Chamran University of Ahvaz, Ahvaz, 6135743135, Iran*

(Received 25 March 2023; revised 11 May 2023; accepted 2 August 2023; published 30 August 2023)

In addition to spin and valley degrees of freedom, a bilayer of transition-metal dichalcogenides (TMDs) exhibits a further degree of freedom, the layer pseudospin, which is associated with the interlayer dynamics. Here, we study, over a wide range of energies, the conditions for the generation and control of the perfect-spin-, valley-, and layer-polarized transport in a nonmagnetic/ferromagnetic/nonmagnetic junction fabricated in AB-stacked bilayer TMDs. We find that, via breaking the inversion and time-reversal symmetries through application of external electric and exchange fields, layer-, perfect-spin-, and valley-polarized transport can be achieved and controlled electrically and magnetically. Analyzing effects related to the band structure and the local density of states, the predictions are rationalized, and in particular we expose the role of tuning the band gap and adjusting the charge localization in one specific layer. Within an appropriate parameter regime, an energy interval with contributions from both layers is identified, leading to enhancement of the transmission and conductance. Our results can be useful for pseudospintronic applications in bilayer TMD-based devices.

DOI: 10.1103/PhysRevApplied.20.024075

I. INTRODUCTION

Monolayers of transition-metal dichalcogenides (TMDs) with a honeycomb lattice structure have two similar but distinguishable valleys which are located at the corners of the first hexagonal Brillouin zone [1] and labeled by K and K'. These valleys are connected by time-reversal (TR) symmetry [2], resulting in Kramers degeneracy of the band structure of TMDs, i.e., states labeled by $K\uparrow$ ($K\downarrow$) are degenerate with those labeled by $K'\downarrow$ ($K'\uparrow$), where ↑ (↓) stands for the spin-up (spin-down) quantum numbers. In TMDs, the low-energy physics takes place in the vicinity of the K and K' valleys (Dirac points) of the conduction and valence bands, which are mostly formed from the d_{z^2} and $d_{x^2-y^2}$, d_{xy} orbitals of the transition-metal atoms, respectively [3,4].

The particular dispersion and the coupling between spin-orbital and valley degrees of freedom in TMDs are the key for technologically interesting phenomena such as spin filtering [5], magnetoresistance [6,7], spin Hall effect [8,9], and topological properties [10,11], or condensate structures [12]. In contrast to pristine graphene, a monolayer of TMDs has a direct band gap of ≈1.7 eV [13] and a remarkable spin-orbit coupling (SOC) strength in the valence band, which makes these systems appealing also for quantum information applications [14]. Numerous studies have addressed the spin- and valley-related phenomena in different TMD-based junctions [6,7,15–19].

In addition to the spin and valley degrees of freedom, carriers in a bilayer of TMDs possess a layer degree of freedom, which can be captured by a pseudospin. In most systems, the layer pseudospin originates from the orbitals and thus couples to the spin via SOC [20]. This feature has attracted a significant amount of interest recently [4,20–24]. Unlike a TMD monolayer, in which the inversion symmetry is broken and the spin and valley degrees of freedom are effectively coupled [2], a bilayer of TMDs is intrinsically inversion-symmetric [25].

There are different ways to control the inversion symmetry in bilayers, such as using electric [4], magnetic [4], or Zeeman fields [26]. In AB-stacked bilayer TMDs, both spin and valley degrees of freedom are coupled to layer pseudospin [4]. Because of the 180° rotation in AB stacking, the out-of-plane spin splitting has a sign that depends on both valley and layer pseudospins [20]. This spin-layer locking offers the opportunity for the manipulation of spins via gate control of layer localization [4]. Additionally, the existence of interlayer coupling may allow easier tuning of the band gap via electrical modulation in bilayer TMDs than in monolayer form with a marked influence on the spin, valley, and layer polarizations in the bilayer TMDs. These aspects are discussed below in detail.

---

[*] yaserhajati@gmail.com

© 2023 American Physical Society

Van Duppen and Peeters [27] investigated the four-band tunneling in bilayer graphene and showed that, for high energies, two modes of propagation exist, and scattering between these two modes can be observed. Recently, the spin, valley, and layer pseudospin transport in a magnetoelectric barrier on AB-stacked bilayer MoS_2 has been studied [28]. It is found that perfect spin-valley polarizations and good layer localization of electrons can be obtained. These polarizations are adjustable by tuning the electric fields.

In contrast to spin- and valley-dependent transport in monolayer TMDs [7,29,30], the spin-valley-layer transport in bilayer form, especially in the presence of an exchange field, has not yet been fully clarified. An important issue in this regard is that the spin-layer locking in AB-stacked bilayer TMDs permits electrical manipulation of spins through controlling layer polarization [20], which is of importance for pseudospintronics.

The present study is devoted to exploring the spin-, valley-, and layer-polarized transport in a nonmagnetic/ferromagnetic/nonmagnetic (N-F-N) junction in AB-stacked bilayer TMD in the presence of electric and exchange fields (cf. Fig. 1). Because of the considerable SOC strength and interlayer coupling in TMDs, by breaking the inversion and TR symmetries upon applying external electric and exchange fields, conditions allowing for perfect spin, valley, and layer polarization can be achieved over a wide energy region. Additionally, applying a perpendicular electric field allows control of the band gap and layer splitting in the junction. Depending on the applied electric fields, one can achieve a situation where both layers or one of them contribute to the transport. These findings might be helpful in designing efficient pseudospintronic devices.

II. MODEL AND THEORY

As for a monolayer of TMDs, for a bilayer the orbitals of metal atoms contribute dominantly to both the valence- and conduction-band edges near the Dirac points [4]. Thus, the low-energy Hamiltonian H_{η,s_z} of TMD bilayers in the presence of electric and magnetic exchange fields can be obtained by adding the interlayer coupling ($t_\perp$) to the $\mathbf{k}\cdot\mathbf{p}$ Hamiltonian of monolayer TMDs while accounting for the coupling to the relevant fields. In doing so we obtain [4,28]:

$$H_{\eta,s_z} = \begin{pmatrix} A_1 & k^+ & 0 & 0 \\ k^- & A_2 & 0 & t_\perp \\ 0 & 0 & A_3 & k^- \\ 0 & t_\perp & k^+ & A_4 \end{pmatrix}. \quad (1)$$

Here we have introduced the notation for the diagonal elements, $A_1 = \Delta - \eta s_z\lambda_c + V + s_z h + U$, $A_2 = -\eta s_z\lambda_v + V + s_z h + U$, $A_3 = \Delta + \eta s_z\lambda_v - V + s_z h + U$, and $A_4 = +\eta s_z\lambda_v - V + s_z h + U$, and we use the basis $\{|d^{\mu}_{z^2}\rangle, (1/\sqrt{2})(|d^{\mu}_{x^2-y^2}\rangle - i\sigma_z|d^{\mu}_{xy}\rangle)\}$, where μ is the layer index and σ_z is the z component of the Pauli matrix. Finally, $k^{\pm} = \hbar v_f(\eta k_x \pm ik_y)$, where k_x and k_y are the perpendicular and parallel wave-vector components, respectively.

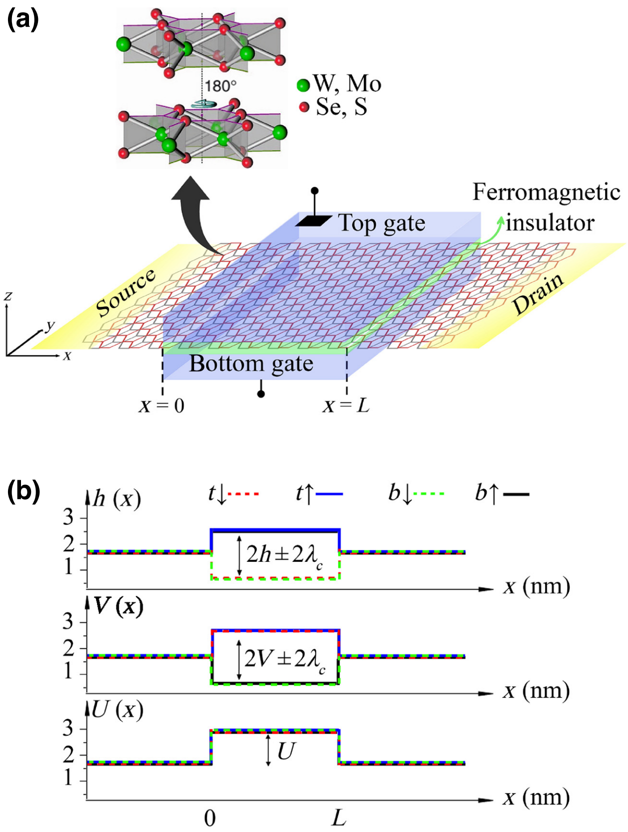

FIG. 1. (a) Schematic illustration of an N-F-N junction based on an AB-stacked bilayer TMD. The side view of the bilayer is shown schematically (with exaggerated splitting between two layers) in the top left, in which the bottom layer is rotated by 180° with respect to the top one, a manifestation of AB stacking. The light green (blue) part shows the ferromagnetic layer (gate application) schematically. The two potential gates can tune the on-site potentials of the layers and also induce a perpendicular electric field in the middle region. (b) The exchange field (top), electric field (middle), and gate voltage (bottom) profiles along the x direction. Here the "t" and "b" refer, respectively, to the top and bottom layers of the conduction band at the K valley of WSe_2.

In Eq. (1), h refers to the energy contribution due to the proximity-induced exchange field (see Sec. IV for more details); Δ is the band gap; U is the gate voltage; V is the scalar potential energy caused by the perpendicular electric field E_z; $\eta = \pm 1$ ($s_z = \pm 1$) indicates the valley (spin) states; λ_c (λ_v) refers to the SOC contribution in the conduction (valence) band; and v_f is the Fermi velocity in TMDs, which is 5×10^5 m/s for WSe_2 and 5.3×10^5 m/s for MoS_2. In this study, we consider the external electric field to be perpendicular to the TMD sheet. Since the d_{z^2} orbital is dominant in the conduction band, $t_\perp$ does not appear in this band. Note that the 180° rotation of layers results in different signs of the SOC for two layers in this model.

The eigenstates of H_{η,s_z} can be written as

$$\mathbf{\Psi}_{\mu,\lambda}(\mathbf{r}) = \frac{e^{i\mathbf{k}\cdot\mathbf{r}}}{E_N}\begin{pmatrix} \hbar v_f\,\mathbf{k}(A_3 - E^{\eta,s_z}_{\mu,\lambda})t_\perp \\ (-A_1 + E^{\eta,s_z}_{\mu,\lambda})(A_3 - E^{\eta,s_z}_{\mu,\lambda})t_\perp \\ F(\hbar v_f\,\mathbf{k}) \\ F(-A_3 + E^{\eta,s_z}_{\mu,\lambda}) \end{pmatrix}, \tag{2}$$

in which λ is the band index, with values 1 for the conduction band and -1 for the valence band, $|\mathbf{k}| = \sqrt{\eta k_x^2 + ik_y^2}$, and $E^{\eta,s_z}_{\mu,\lambda}$ are the spin-valley-layer-dependent eigenvalues of H_{η,s_z}, which we discuss in detail in the Appendix. The other parameters appearing in Eq. (2) read

$$F = (A_2 - E^{\eta,s_z}_{\mu,\lambda})(E^{\eta,s_z}_{\mu,\lambda} - A_1) + (\hbar v_f\,k)^2 \tag{3}$$

and

$$\begin{aligned} E_N = \{&(\hbar v_f\,k)t_\perp(A_3 - E^{\eta,s_z}_{\mu,\lambda})^2 + (A_3 - E^{\eta,s_z}_{\mu,\lambda})(E^{\eta,s_z}_{\mu,\lambda} - A_1)^2 t_\perp^2 \\ &+ ((\hbar v_f\,k)F)^2 + F^2(A_3 - E^{\eta,s_z}_{\mu,\lambda})^2\}^{1/2}. \end{aligned} \tag{4}$$

Considering $\Psi_{(1,2,3)}$ as the wave functions for each region with appropriate boundary condition at the borders, i.e., at $x = 0, L$, leads to

$$\begin{aligned} \Psi(k_1^{+(-)}) + r_1\Psi(-k_1^-) + r_2\Psi(-k_1^+) &= A\Psi(k_2^+) \\ + B\Psi(-k_2^+) + C\Psi(k_2^-) &+ D\Psi(-k_2^-) \end{aligned} \tag{5a}$$

and

$$\begin{aligned} A\Psi(k_2^+) + B\Psi(-k_2^+) &+ C\Psi(k_2^-) + D\Psi(-k_2^-) \\ &= t_1\Psi(k_3^+) + t_2\Psi(k_3^-), \end{aligned} \tag{5b}$$

in which $k_{1,2,3}$ are the wave vectors in each triple of the regions, and L is the length of the middle region, which is fixed to 10 nm during this work. Because of the translational invariance in the y direction, k_y is a good quantum number, and hence transmission coefficients $(t^{+,-}_{1,2})$ are obtained by solving Eqs. (5a) and (5b). Then, the transmission probability can be found as

$$T_{11,12,21,22} = \zeta |t^{+,-}_{1,2}|^2, \tag{6}$$

where $\zeta = k^{+(-)}_{1,x}/k^{-(+)}_{1,x}$, in which we have used the fact that $k_1 = k_3$ in an N-F-N junction.

Corresponding to the two distinct wave vectors $k^\pm$ in the first (incoming) and third (outgoing) regions, four distinct channels are relevant for the transmission, which are listed in Table I. When the wave vector of the incoming and outgoing carriers are the same, the channels are called nonscattering modes (which have been named T_{11} and T_{22}), while the channels in which the incoming wave vector changes during transmission through the barrier are named scattering modes (shown by T_{12} and T_{21} in this study). Because of the similarity between the incoming and outgoing carriers' wave vectors in nonscattering modes, they are expected to be the dominant channels for transmission. When $E < \Delta$, the wave vector k_1 (which is equal to k_3 in this N-F-N junction) becomes imaginary. Thus, we restrict our assumption to $E > \Delta$ for transmission.

TABLE I. Different transmission channels based on different incoming and outgoing modes in bilayer TMDs.

Incoming mode	Outgoing mode	Mode type	Shown by
k^+	k^+	Nonscattering	T_{11}
k^+	k^-	Scattering	T_{12}
k^-	k^+	Scattering	T_{21}
k^-	k^-	Nonscattering	T_{22}

The spin-valley-resolved conductances are calculated using the Landauer-Büttiker formalism as [31]

$$G_{\eta,s_z} = G_0 \int T_{(11,12,21,22)\eta,s_z}\,dk_y, \tag{7}$$

where $G_0 = e^2 W k_1/(2\pi h)$ is the reduced unit of conductance with the system width of W.

In Table II, we list and compare the most important structural properties of two TMDs, i.e., WSe_2 and MoS_2. Evidently, both of them have a suitable band gap and almost the same lattice parameter. However, the Mo-based one shows weaker SOC at both valence and conduction bands because of the different atomic weights and sizes [35]. We only investigate two members of the TMD family here: MoS_2 as the first-discovered one and WSe_2 as the one with heavier atoms and more relevance for applications and low cost [35] (compared to Te, for example). From the similar structural properties of WS_2 and $MoSe_2$ (not shown), we expect that a similar behavior can be found in these materials.

It should be noted that, although the band gap in bilayer TMDs is indirect, the gate voltage can modify the energy-level structure. For instance, applying a positive (negative) gate voltage is reflected as a spin-valley-independent

TABLE II. A comparison between MoS_2 and WSe_2. Data are taken from Refs. [6,7,23,32–34].

TMD	a_0 (Å)	Band gap (eV)	λ_c (meV)	λ_v (meV)	$t_\perp$ (meV)
WSe_2	3.32	1.7	7.5	112.5	67
MoS_2	3.16	1.66	0	37.5	43

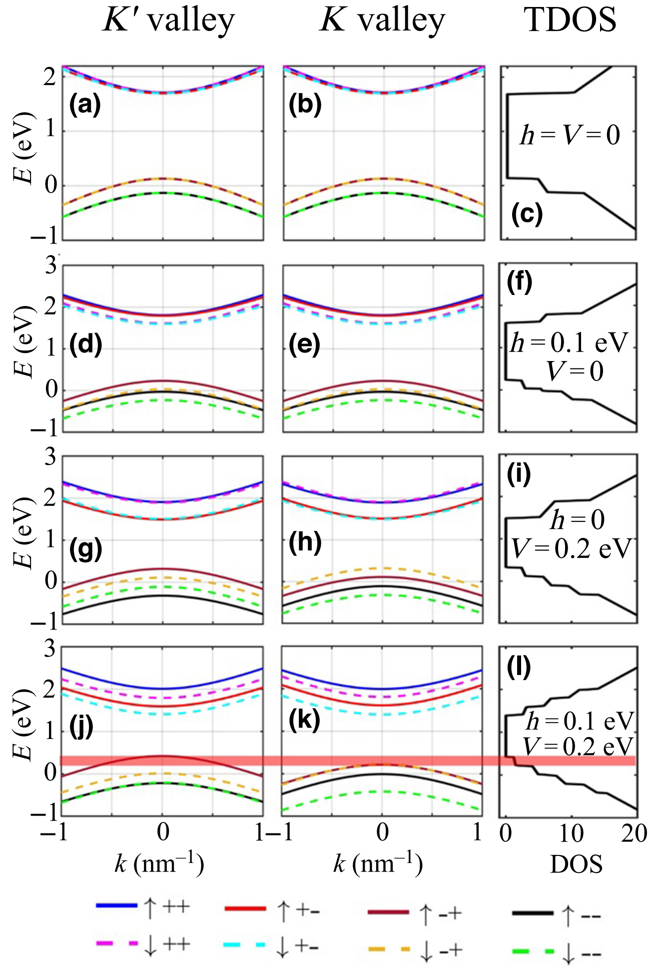

FIG. 2. Band structure and total density of states of the middle region in a WSe$_2$-based junction for (a)–(c) $h = V = 0$, (d)–(f) $h = 0.1$ eV, $V = 0$, (g)–(i) $h = 0$, $V = 0.2$ eV, and (j)–(l) $h = 0.1$ eV, $V = 0.2$ eV. The left column indicates the K' valley, the middle one is for the K valley, and the right column refers to TDOS, which is the sum of both valleys. The red-shaded area shows the energies in which only one band exists and the condition for perfect polarization is satisfied.

external tuning parameter for the effective Hamiltonian of bilayer TMDs: all the energy bands shift upward (downward), simultaneously. In the normal regions [cf. Figs. 2(a) and 2(b)], electrons originate from the conduction-band minimum at the K or K' point. However, in the middle region, the gate voltage shifts the bands upward in such a way that the valence-band maximum at these points contribute to transport. This condition can be achieved for different states when $U \geq \Delta \pm (\lambda^2 + t_\perp^2)$ is applied, assuming $h = 0$. Therefore, we have considered $U > 1.9$ eV to ensure that transport is governed by the valence band in the barrier where the effect of SOC is strong.

Our study is focused on the quasimomentum near the K or K' point due to the large separation between this point and other high-symmetry points in wave-vector space of bilayer TMDs (e.g., the Γ point). This reasoning only holds at low temperatures, where the shift of the band structure due to phonon effects is small [36], as we assume here. Based on this approximation, the Landauer-Büttiker formalism is reasonably applicable (for similar studies, we refer, for example, to Ref. [28] for bilayers of MoS$_2$ and to Ref. [27] for graphene).

III. RESULTS AND DISCUSSION

Figure 1(a) illustrates the proposed bilayer-TMD-based N-F-N junction. The electron is launched from the left normal region (source) and is detected at the drain part in the right normal region. In the middle region of length L, the application of the local exchange field (h), gate voltage (U), and electric field (E_z) manipulate the band structure, providing an opportunity for transport control. A double gate structure, consisting of top and bottom gates, can be utilized to control the normal electric field, similar to the approach proposed in Ref. [28]. As seen in the top left of Fig. 1(a), the lower layer is rotated 180° with respect to the upper one, which is a manifestation of AB stacking. The substrate can be replaced by a ferromagnetic layer to proximity-induce ferromagnetism [37]. Similar junctions based on TMD monolayers have been studied extensively [13,16,29,30,38,39].

Figure 1(b) shows the exchange field, electric field, and gate profile along the x axis for the conduction band of the K valley of WSe$_2$. For simplicity, we have restricted this figure to only the K valley. All the controlling tools, including the exchange field, gate voltage, and normal electric field, are locally applied in the barrier region, which has a length of L. Outside the barrier region, i.e., at $x < 0$ and $x > L$, the Kramers degeneracy is evident due to the presence of SOC and the inversion-symmetric nature of the TMD bilayer. The gate voltage is independent of spin, valley, and layer, and moves all the bands upward or downward. However, the exchange (electric) field is coupled to the spin (layer) index and thus enhances the splitting of different spin (layer) states. Note that a similar graph is obtained for another valley with slight differences, due to the different SOC sign.

To illustrate the effect of the applied fields on the bands, we show the band structure of the middle region in a WSe$_2$-based junction with respect to the wave vector for different parameter regimes in Fig. 2. Briefly, the following conclusions can be reached.

(i) In the absence of all fields, i.e., $h = U = V = 0$, spin splitting due to SOC cannot be seen in either the conduction or the valence band, which means $E_{K\uparrow} = E_{K'\uparrow} = E_{K\downarrow} = E_{K'\downarrow}$ for each layer, due to the inversion and TR symmetries in bilayer WSe$_2$; a kind of Kramers degeneracy. However, the bands of different layers show a splitting of 262 meV ($2\lambda_c = 15$ meV) at the valence (conduction) band of WSe_2 due to the different signs of intrinsic SOC at the two layers and also the effect of interlayer coupling in our model.

(ii) As can be seen in Figs. 2(d) and 2(e), when h is finite, the spin degeneracy is broken such that it shifts the spin-up bands of both layers upward, and shifts the spin-down bands downward, leading to a spin splitting of $2h$ in both layers. Because of the inversion symmetry, applying h individually does not cause an imbalance between the two valley states. Thus, still $K\uparrow(\downarrow) = K'\uparrow(\downarrow)$ for each layer. Thanks to the relatively strong SOC of WSe_2, we observe eight separate bands in each valley. Moreover, stronger SOC in the valence band results in an asymmetry between the conduction and valence bands, which is also seen in Figs. 2(a) and 2(b).

(iii) When only the perpendicular electric field is switched on ($V \neq 0$), the layers are separated due to the fact that, in our model, V admits different signs in the two layers [see Figs. 2(g) and 2(h)]. Thus, V shifts one layer upward while shifting the other one downward, leading to a layer splitting of $2V$. As for h, applying V alone cannot break all the degeneracies. Because of the TR symmetry, we still have $K\uparrow = K'\downarrow$.

(iv) When only the gate voltage U is applied to the system, both TR and inversion symmetries are preserved and it only shifts the bands upward or downward, as indicated in Refs. [6,40] (not shown here).

(v) Applying both V and h simultaneously breaks both inversion and TR symmetries, and, thanks to the SOC and interlayer coupling of bilayer TMDs, it lifts all the degeneracies, leading to 16 separate energy bands [see Figs. 2(j) and 2(k)]. Hence, a condition can be found in which only one band from a certain spin-valley-layer state touches the Fermi level, which is essential for perfect polarization [see the red-shaded area in Figs. 2(j) and 2(k)]. Clearly, the splitting in the valence band is much more pronounced due to the stronger SOC and the existence of the interlayer coupling in this band.

We note that it is possible to achieve the band diagram for MoS_2 only by substituting $\lambda_c = 0$, $\lambda_v = 37.5$ meV, $v_f = 5.3 \times 10^5$ m/s, $t_\perp = 43$ meV, and $\Delta = 1.66$ eV, which is not shown here.

In the right column of Fig. 2, we show the total density of states (TDOS) of bilayer WSe_2 for different parameter regimes coinciding with the band structure. Similar to what is seen in the band structure, the stronger SOC in the valence band causes an asymmetry in TDOS diagrams, which is more visible in Fig. 2(c) when $V = h = 0$. Evidently, when the Fermi energy becomes equal to the energy of one band (or more), the TDOS curve shows a step. At high energies, in which all the bands have touched the Fermi level, the TDOS is almost linearly proportional to the energy. In the absence of fields (i.e., $h = V = 0$), the TDOS in the conduction band shows only one step due to the weak SOC in this band. However, as inferred from Fig. 2(f), when $h \neq 0$, the steps in TDOS increase due to the spin splitting caused by h. A similar behavior can be seen in Fig. 2(i) when $V \neq 0$, due to the layer splitting caused by V. All the TDOS diagrams are in agreement with the corresponding band structure and also with what is reported in Ref. [22].

To inspect the effects of electric and exchange fields on the electron transmission of the proposed junction, we have calculated the resolved transmission probabilities ($T_{11}, T_{12}, T_{21}, T_{22}$) for both spin states at the K valley, as a function of electric field and incident (Fermi) energy E. The results for MoS_2, at normal electron incidence ($k_y = 0$), are presented in Fig. 3. Note that, here, we restrict the energies to the valence band because the SOC in the valence band is substantially stronger than that of the conduction band, and also the interlayer coupling affects only the valence band.

First of all, the domination of nonscattering modes, i.e., T_{11} and T_{22}, can be seen. Comparing Figs. 3(a)–3(d) with Figs. 3(e)–3(h) shows a mirror symmetry between spin-up and spin-down transmissions. Because of the TR symmetry, even in the presence of V, we can see that $K\uparrow(\downarrow) = K'\downarrow(\uparrow)$. Thus, we depict only the K-valley transmission in Fig. 3, which is equal to that of K' with opposite spin. The sum of all resolved transmissions is captured in Figs. 3(i) and 3(j). Evidently, the total transmissions show a great agreement with the band structure (white dashed lines). Since increasing V enhances the layer splitting [see Figs. 2(g) and 2(h) and its related explanation], the splitting of the white bands in Figs. 3(i) and 3(f) enhances by increasing $|V|$. In the absence of V ($V = 0$), the bands show a splitting of $2\sqrt{t_\perp^2 + \lambda_v^2} = 114$ meV, which originates from the intrinsic SOC and interlayer coupling.

Also, the relatively strong SOC of MoS_2 shifts the minimum-distance point, which is shown by the white double arrow in Figs. 3(i) and 3(j), toward $V > 0$ ($V < 0$) for the spin-up (spin-down) electrons. In other words, the minimum distance between the bands is located at $V = \pm\lambda_v = \pm 37.5$ meV for MoS_2. At certain values of V in which $E < U - \sqrt{(\lambda_v - V)^2 + t_\perp^2}$ is satisfied, both layers contribute to the transport, thus $T > 1$ occurs. The same behavior can be seen for the spin-down state with different regions of energy, i.e., when $E < U - \sqrt{(\lambda_v + V)^2 + t_\perp^2}$.

The density plots of the resolved transmissions of WSe_2 with respect to V and incident (Fermi) energy are shown in Figs. 4(a)–4(h). Similar to MoS_2, the domination of nonscattering modes is seen in this material. However, different SOC and band gaps lead to different energy ranges in which the transmission vanishes for each channel. The mirror symmetry when changing the spin state is evident, which means that for T_{11} nonzero spin-up contributes

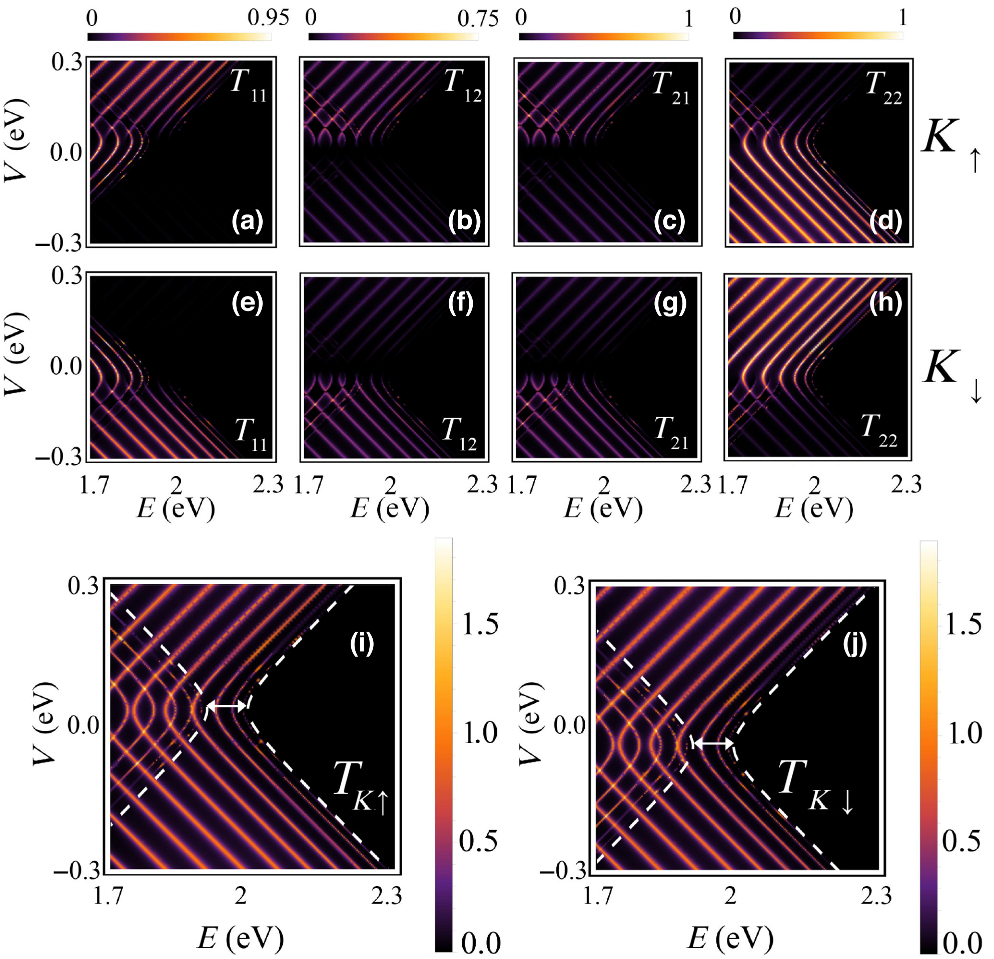

FIG. 3. (a)–(h) Density plots of resolved transmission probability of MoS_2 under $U = 1.95$ eV with respect to electric field V and incident (Fermi) energy at $h = 0$ for $K\uparrow$ (a)–(d) and $K\downarrow$ (e)–(h). The transmission channels are labeled in each panel. (i),(j) Total transmission probability ($T_{11} + T_{12} + T_{21} + T_{22}$) for $K\uparrow$ (i) and $K\downarrow$ (j). The white dashed lines denote the band structure with respect to V at $k = 0$.

mostly for $V > 0$, while nonzero spin-down contributes mostly for $V < 0$. The inverse behavior applies to T_{22}.

The behavior of scattering modes is almost the same because of the small difference between k^+ and k^- in this situation. Stronger SOC leads to wider splitting between the two layers at $V = 0$. Hence, a splitting of $2\sqrt{t_\perp^2 + \lambda_v^2} =$ 262 meV is observed in WSe_2 (which is larger than the 114 meV that is found for MoS_2 in Fig. 3). Also, the minimum-distance point is shifted more than for MoS_2 (the minimum point is located at $V = \pm 112.5$ meV for WSe_2, as shown by the white double arrow), leading to different energy intervals in which both layers contribute to the transmission. Analogous to MoS_2, an oscillatory behavior with respect to energy is observed for the total and resolved transmissions, which can be attributed to the wave-vector quantization, fulfilled when $k_{2,x}L = n\pi$. Since the barrier's wave vector depends on electric field V, varying V also obeys the quantization condition, and an oscillatory behavior with different patterns is observed with respect to V in both materials [see Figs. 3(i) and 3(j) and Figs. 4(i) and 4(j)].

Figures 3(i) and 3(j) and Figs. 4(i) and 4(j) illustrate the effect of V on the band gap. Comparing Figs. 4(i) and 4(j) shows that increasing $|V|$ decreases the total gap, which can be traced back to the different signs of V in the two layers. More precisely, applying V leads to a splitting of $\sqrt{t_\perp^2 + (V + \lambda_v)^2}$ between the two layers, and thus the transmission gap is reduced. Moreover, due to the SOC and interlayer coupling of TMDs, the total transmission for spin-up shows a mirror symmetry versus V with respect to that of the spin-down [see Figs. 3(i) and 3(j) and Figs. 4(i) and 4(j)]. This effect is useful for transport control of the junction.

Up to now, we have considered only the conditions in which $h = 0$ and only the gate voltage and the electric field are applied to the middle region. Now, we aim to explore

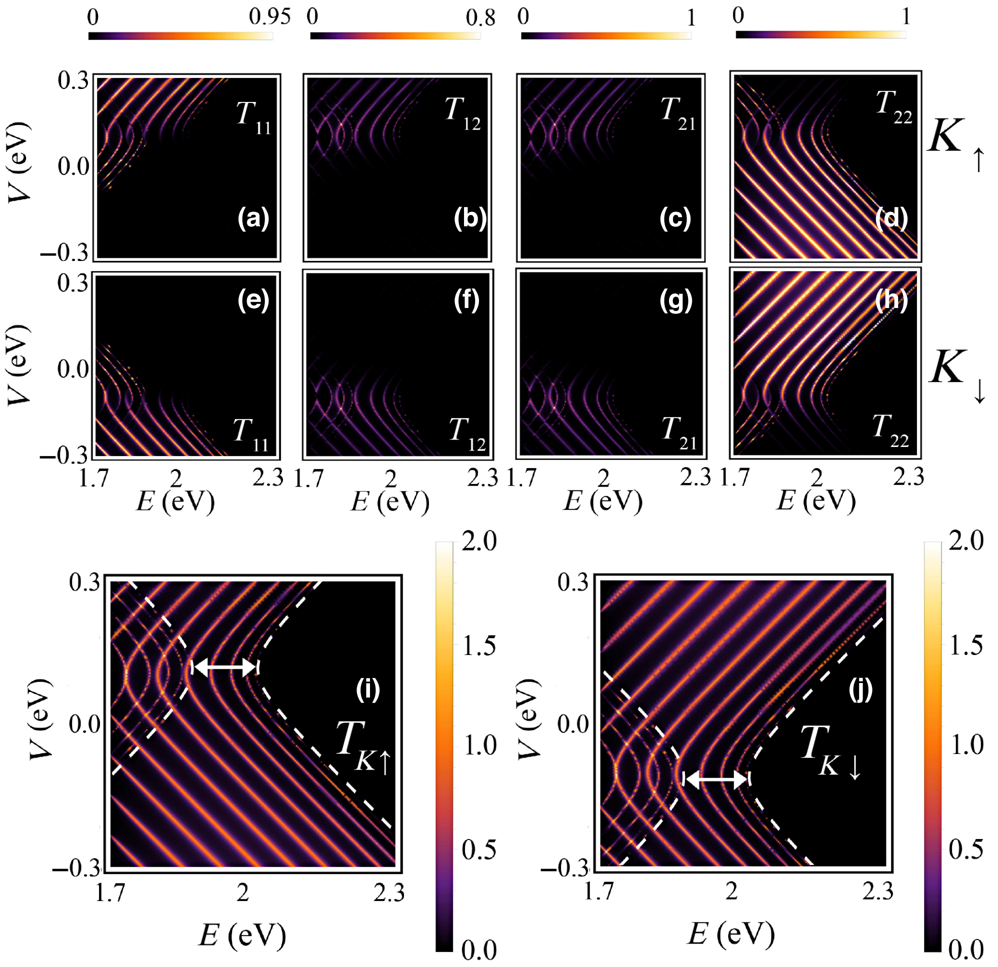

FIG. 4. (a)–(h) Density plots of resolved transmission probability of WSe$_2$ under $U = 1.95$ eV with respect to electric field V and incident (Fermi) energy at $h = 0$ for $K\uparrow$ (a)–(d) and $K\downarrow$ (e)–(h). The transmission channels are labeled in each panel. (i),(j) Total transmission probability for $K\uparrow$ (i) and $K\downarrow$ (j). The white dashed lines denotes the band structure with respect to V at $k = 0$.

the effect of the exchange field in addition to electrical modulations. The calculated total spin-valley-resolved transmissions for both TMDs, WSe$_2$ and MoS$_2$, at $h = V = 0.1$ eV are shown in Figs. 5(a) and 5(b), respectively.

As inferred from the band structure in Fig. 2, applying h and V simultaneously can break both the inversion and TR symmetries. Consequently, by varying the energy, an area is found in which only one band from a certain valley, spin, and layer touches the Fermi level, leading to a perfect-spin-, valley-, and layer-polarized transport [the red shaded regions in Figs. 5(a) and 5(b)]. Comparing Figs. 5(a) and 5(b) shows that the polarized region in WSe$_2$ is wider than in MoS$_2$ due to stronger SOC and interlayer coupling of WSe$_2$, as compared to MoS$_2$. We restrict the energy region to the valence band due to the domination of SOC and interlayer coupling in this band. As a consequence, modulation of the valence band in bilayer TMDs is a promising way for spintronic or valleytronic applications.

Analytically, when the energy satisfies the condition $\sqrt{(V+\lambda_v)^2+t_\perp^2}+U+h < E < \sqrt{(V-\lambda_v)^2+t_\perp^2}+U+h$, which is equivalent to 2.118 eV $< E <$ 2.273 eV for WSe$_2$ and to 2.126 eV $< E <$ 2.194 eV for MoS$_2$, the transport becomes fully spin-valley-layer-polarized. This means that in WSe$_2$ we have a region of 155 meV for polarized transport, while in MoS$_2$ this area is about 68 meV, confirming the advantage of using WSe$_2$ as a material for spintronics, valleytronics, or pseudospintronics.

Comparing Figs. 5(a) and 5(d) [or Figs. 5(b) and 5(c)] shows that, when the first band of each layer touches the Fermi level, a nonzero transmission appears in the T diagram. After that, by the intersection between the second band of that layer with the Fermi level while varying the energy, the transmission is allowed to surpass unity, due to the contribution of both layers. Thus, the electric and exchange modulations can control the flow of carriers, their state, i.e., from which spin, valley, or layer transmission can occur, and also the transmission

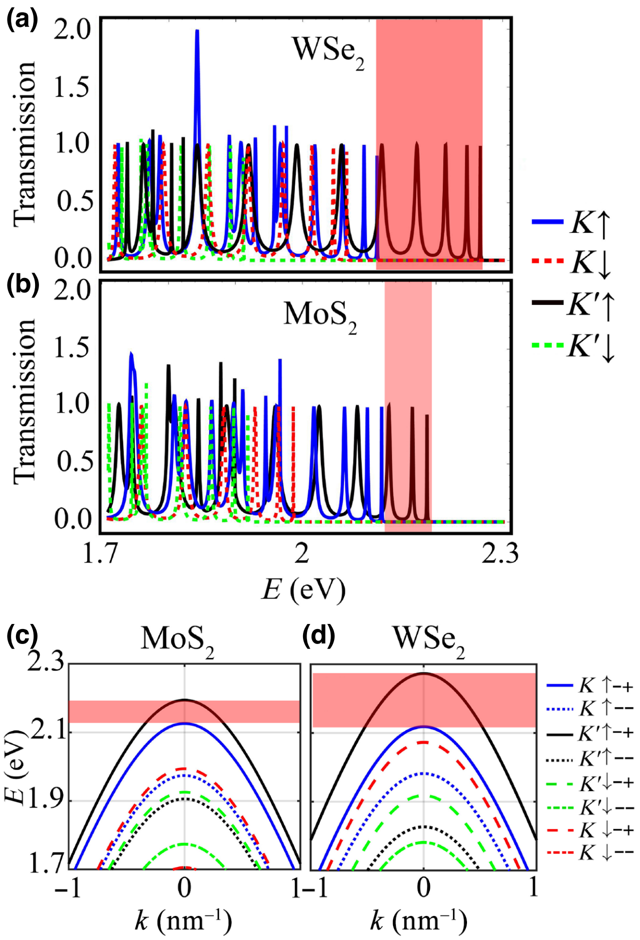

FIG. 5. (a),(b) Spin-valley-resolved transmissions with respect to energy for (a) WSe_2 and (b) MoS_2 at $h = V = 0.1$ eV. (c),(d) The corresponding band structure for the valence bands of (c) MoS_2 and (d) WSe_2. Here, $U = 1.95$ eV and the left (right) plus sign or minus sign in the legend on the right indicates the valence band (top layer) or conduction band (bottom layer).

probability (which is limited to or exceeds unity).

To further study the effect of the electric and exchange fields on the density probability and polarizations in the real space of three regions, we have depicted the local density of states (LDOS) and triple polarizations in Fig. 6 for different parameter regimes of the MoS_2-based device. Here, we have chosen the space interval of -7 to 7 nm along the x direction to cover all regions, and also set the energy in the range of 1.75 to 2.25 eV, which corresponds to the valence band of TMDs. Evidently, when all the fields are switched off, the density of states is almost zero in the barrier, but finite in the normal regions. Additionally, in the absence of the electric and exchange fields, i.e., $h = V = 0$, both inversion and TR symmetries are preserved and lead to a nonpolarized transport, as seen in the first row of Fig. 6.

The second row of Fig. 6 shows that applying the exchange field of 0.1 eV causes a spin imbalance, and thus a remarkable (almost perfect) spin polarization can be detected at the edge of the valence band at all values of k for $-5 < x < 5$ that belongs to the middle region. However, the valleys or layers are still degenerate because h by itself cannot break all the symmetries, and consequently the valley and layer polarizations vanish.

Using $V = 0.2$ eV when the exchange field is switched off results in inversion symmetry breaking. An almost perfect layer polarization without a considerable spin or valley polarization is observed, as shown in the third row of Fig. 6. In fact, when V is applied, we identify an interval of energy for which only the bands of one layer (from both spins and both valleys) touch the Fermi level, resulting in almost perfect layer polarization.

When both V and h are applied to the barrier region, the former breaks the layer degeneracy, and the latter lifts the spin degeneracy and hence, thanks to the SOC of TMDs, both inversion and TR symmetries are broken. So, all the polarizations become substantial (almost perfect) at the edge of the bands, which is in agreement with the band structure shown in Fig. 2. Additionally, comparing the first and third rows of Fig. 6 indicates the effect of V on the reduction of the band gap, which is a useful tool to control the transport properties of the junction. It can be observed that the zero LDOS at the barrier region in the absence of electric and exchange fields changes to a finite LDOS by applying $V = 0.2$ eV. This observation is explained by the layer-dependent sign of V that causes the enhancement of layer splitting and consequently a reduction of the gap.

Similar observations are made for WSe_2 in Fig. 7. Different band gaps, interlayer couplings, and SOC in WSe_2 change the location of bands and consequently lead to different polarizations of this material, as compared to MoS_2. The stronger SOC and interlayer coupling in WSe_2 offer more accessible conditions for achieving perfect polarizations. Also, the stronger SOC and the interlayer coupling can be utilized for the reduction of the band gap, as compared to the MoS_2-based device. Thus, in WSe_2 a finite LDOS can be seen in the middle region even in the absence of all fields (see the first row of Fig. 7). These features lead to the observation that applying $V = 0.2$ eV on the WSe_2-based device causes more gap reduction in WSe_2, as seen in the third row of Fig. 7.

It must be mentioned that, due to the degeneracy of energy bands in the absence of fields, the LDOS diagram shows a higher density in the middle region, as compared to other conditions depicted in other parameter regimes. This observation is made also for MoS_2 (Fig. 6). Interestingly, when $h = 0.1$ eV and $V = 0.2$ is applied, the valley polarization switches from positive to negative with increasing energy. This is due to the valley switching in the band structure that is seen in Figs. 2(j) and 2(k). It is evident that the intersection between the K-valley bands

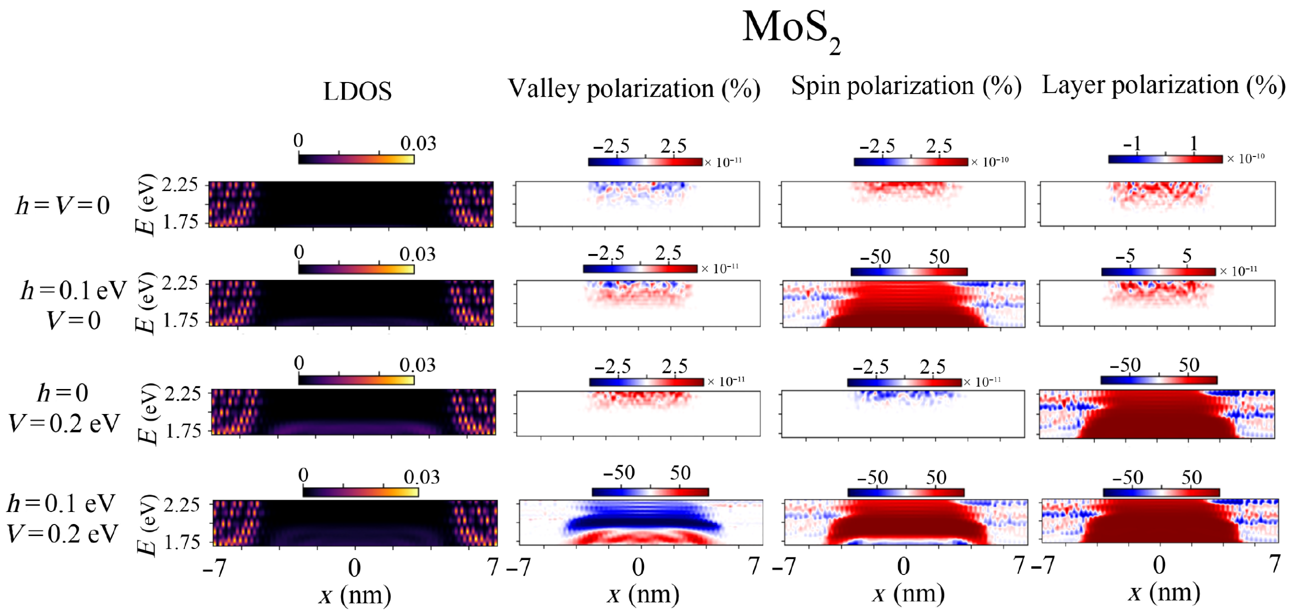

FIG. 6. Local density of states and the corresponding polarizations for different values of h and V of $\mathrm{MoS_2}$ at $U = 1.66$ eV.

vanishes before the K' one. Therefore, at the intersection point of the $K\uparrow$ band, valleys are switched, and thus the sign of the valley polarization changes. Comparing Figs. 6 and 7 shows that this observation is more pronounced in $\mathrm{WSe_2}$, due to the stronger SOC and interlayer coupling. However, when only h is applied, in the considered energy region, only spin-up states from both valleys contribute to the transport and no switching happens in the spin polarization of both materials. A similar scenario occurs for the layer polarization at $V = 0.2$ eV.

The total conductance (summed over all spin-valley-resolved conductances $G_T = \sum_{\eta,s_z} G_{\eta,s_z}$) is shown in Fig. 8 with respect to energy and electric field. Figure 8(a) illustrates the effect of the electric field on the gap region. Evidently, increasing V reduces the gap region, because of the closing of both conduction and valence energy bands due to the different signs of V in the Hamiltonian of each layer. Similar to $\mathrm{MoS_2}$, the gap reduction with V is observable in $\mathrm{WSe_2}$ [Fig. 8(b)]. However, a wider band gap, a stronger SOC, and interlayer coupling of $\mathrm{WSe_2}$ result in a different gap region in the conductance curve. Thus, a wider energy range is needed to see the gap for all values of V. The gap reduction by V is explained by the band structure (Fig. 2). Applying V affects the two

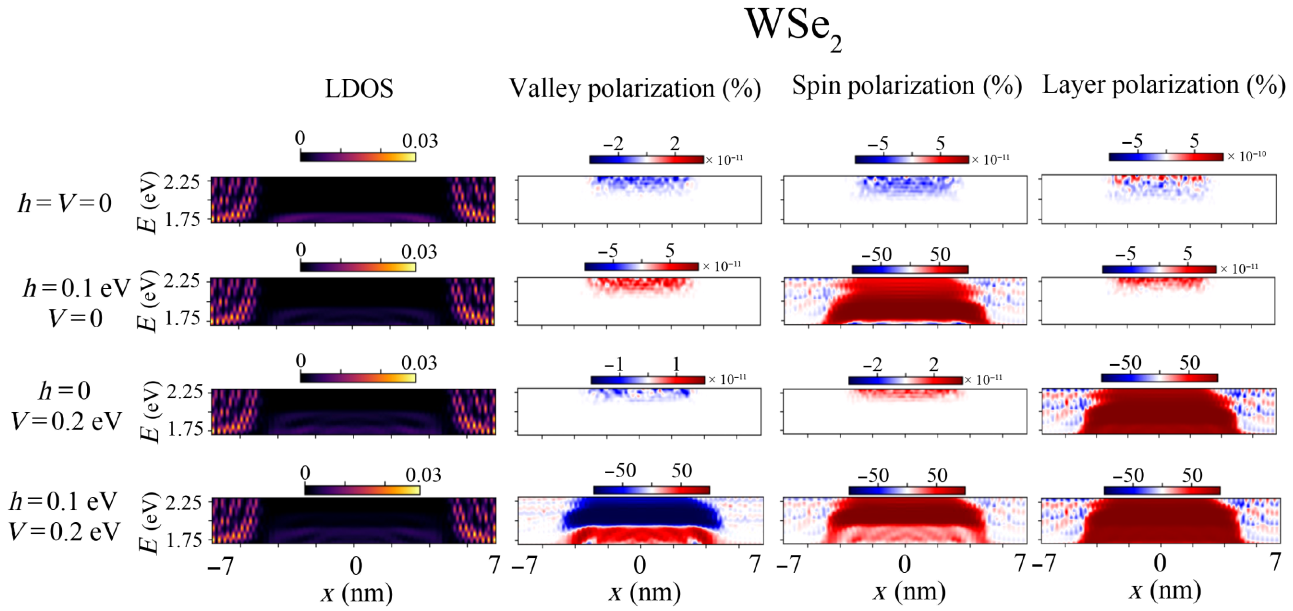

FIG. 7. Local density of states and the polarizations for varying h and V of $\mathrm{WSe_2}$ at $U = 1.7$ eV.

layers differently. One layer is shifted upward and the other downward. Hence, the splitting between the two layers' bands increases with V, resulting in a gap reduction in conductance. The oscillatory behavior of transmission is reflected in a similar conductance behavior for both TMDs.

Increasing the energy [Figs. 8(c) and 8(d)] shifts the intersection point of each spin-valley-layer-resolved band. At higher energies of the valence band, fewer bands touch the Fermi level and therefore the conductance is reduced by increasing E. When the energy exceeds a certain material-dependent value, the Fermi level lies in the band gap for $|V| = 0$. By increasing V, the gap is narrowed and thus the Fermi level touches the bands and the conductance becomes nonzero. A similar argument applies to WSe_2. The field E_z can lead to wave-vector quantization and thus an oscillatory behavior in the conductance.

So far we have fixed L. Increasing L causes a wider area that is affected by electric and exchange fields, which may enhance the polarization [15]. However, L should be smaller than the diffusion length of the TMD to guarantee ballistic transport.

Phonons may affect the electronic characteristics of semiconductors [41]. In our case of electromagnetically modulated bilayer TMDs, the energy scales associated with phonons are smaller compared to other energy scales, e.g., SOC and other electromagnetic modulations used in this work, which are on the order of hundreds of millielectron volts. Therefore, in low-temperature regimes and at short length scales, the single-phonon processes do not lead to a significant band flip or undesired band displacement under electromagnetic modulations. We therefore ignore the phonon's influence on transport properties (e.g., polarizations) and band characteristics, even when the electric and exchange fields are present.

IV. EXPERIMENTAL FEASIBILITY

A monolayer TMD is produced for instance via the mechanical exfoliation method of bulk WSe_2 [20,42], followed by direct transfer onto a suitable substrate. This simple fabrication process avoids degradation of the material by lithographic processes and provides devices with good optical and electrical characteristics [43]. Ferromagnetic proximity effects on TMDs have been widely studied, e.g., Ref. [44]. Different materials such as MnO [45], $BiFeO_3$ [46,47], CrI_3 [48,49], h-VN [50], EuO [51–53], YIG [53], and EuS [44] can be used for the proximity effect.

Experimental evidence of spin, valley, and layer polarization has been reported by recent polarization-resolved photoluminescence and scanning tunneling spectroscopy studies in bilayer WSe_2 [4,20,54]. The perpendicular electric field can be applied externally and tuned via bias voltage. The highest potential energy used in this work is 300 meV, which is well feasible. There are number of methods for detecting the valley polarization, e.g., by using polarization-resolved microphotoluminescence [25]. Similar work is done in the presence of back-gate voltage in Ref. [20]. It is worth mentioning that using the electric

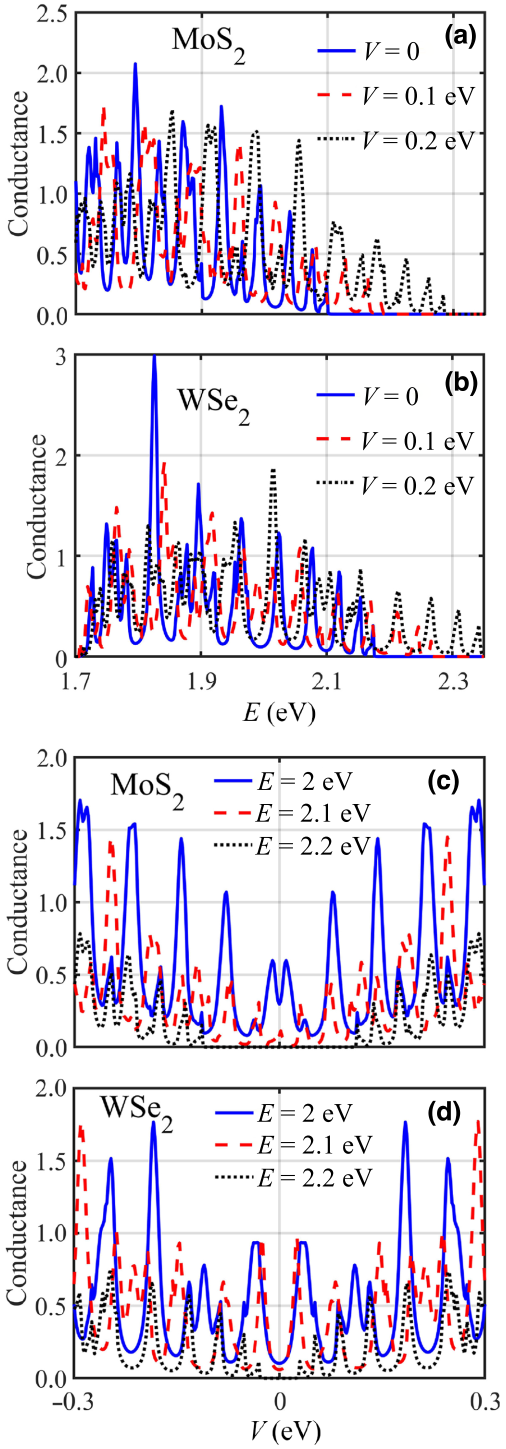

FIG. 8. (a),(b) Total conductance in units of G_0 versus energy for different electric fields, and (c),(d) total conductance in units of G_0 versus electric field at different energies, for (a),(c) MoS_2 and (b),(d) WSe_2 at $U = 1.9$ eV.

field or gate voltage cannot change the bond length and the bond angle of the two-dimensional system [6].

In experiments, disorder, impurities, intervalley scattering, and misalignment of the layers are common limiting factors. Experimental works on $\mathrm{WSe_2}$ indicate that the disorder potential caused by strain and shallow impurity potentials cannot affect much the valley properties in TMD-based junctions [55]. Therefore, we expect our findings to remain qualitatively robust against weak disorder, impurities, and misalignments, with the available experimental techniques where these obstacles can be remedied.

V. CONCLUSIONS

Spin-, valley-, and layer-polarized transport in nonmagnetic/ferromagnetic/nonmagnetic junctions made in an AB-stacked bilayer TMD has been studied while exposing the junction to electromagnetic fields and gate voltage. We found that applying electric and exchange fields can break the inversion and TR symmetries of the bilayer TMD, leading to a situation in which only one band from a specific layer, spin, or valley state intersects the Fermi level. Consequently, a symmetry-adjustable perfect-spin, valley, or layer polarization can be achieved over a wide range of energies and confirmed by the LDOS calculation. Controlling the symmetries via electric and exchange fields renders it possible to tune the gap, offering a way to control the polarizations of the device. Proper tuning of the parameters allows one to control whether only one or both of the layers contribute to the transport. Our findings can be useful in TMD-based spintronic, valleytronic, or pseudospintronic applications.

ACKNOWLEDGMENTS

Y.H. thanks Martin-Luther Universität Halle-Wittenberg for hospitality and support during his visit when this work was done. Y.H. also acknowledges financial support from Iran Science Elites Federation. This work has been supported by the DFG under project No. 328545488 within the SFB TRR227.

APPENDIX: EIGENVALUES OF BILAYER HAMILTONIAN

Solving the eigenvalues of the Hamiltonian leads to the quartic equation

$$E^4 + a_1E^3 + a_2E^2 + a_3E + a_4 = 0, \tag{A1}$$

with

$$a_1 = -(A_1 + A_2 + A_3 + A_4), \tag{A2}$$

$$\begin{aligned} a_2 = {} & A_1A_2 + A_1A_3 + A_2A_3 + A_1A_4 + A_2A_4 + A_3A_4 \\ & - 2k^2 - t^2, \end{aligned} \tag{A3}$$

$$\begin{aligned} a_3 = {} & -A_1A_2A_3 - A_1A_2A_4 - A_1A_3A_4 - A_2A_3A_4 \\ & + (A_1 + A_2 + A_3 + A_4)k^2 + (A_1 + A_3)t^2, \end{aligned} \tag{A4}$$

$$\begin{aligned} a_4 = {} & A_1A_2A_3A_4 - A_1A_2k^2 - A_3A_4k^2 + k^4 \\ & - A_1A_3t^2. \end{aligned} \tag{A5}$$

Solving Eq. (2) results in

$$E^{\eta,s_z}_{\mu,\lambda} = \frac{1}{2}\left(\frac{-a_1}{2} + \lambda\sqrt{X} + \mu\sqrt{\Gamma - \frac{Y^{1/3}}{3\times 2^{1/3}} + \lambda\frac{-a_1^3 + 4a_1a_2 - 8a_3}{4\sqrt{X}}}\right), \tag{A6a}$$

where

$$Y = \kappa + \sqrt{-4(a_2^2 - 3a_1a_3 + 12a_4)^3 + \kappa^2}, \tag{A6b}$$

$$\kappa = 2a_2^3 - 9a_1a_2a_3 + 27a_3^2 + 27a_1^2a_4 - 72a_2a_4, \tag{A6c}$$

$$\begin{aligned} X = {} & \frac{a_1^2}{4} - \frac{2a_2}{3} + \frac{(2^{1/3})a_2^2 - 3a_1a_3 + 12a_4}{3Y^{1/3}} \\ & + \frac{Y^{1/3}}{3\times 2^{1/3}}, \end{aligned} \tag{A6d}$$

$$\Gamma = \frac{a_1^2}{2} - \frac{4a_2}{3} - \frac{(2^{1/3})a_2^2 - 3a_1a_3 + 12a_4}{3Y^{1/3}}. \tag{A6e}$$

[1] H. Ochoa and R. Roldán, Spin-orbit-mediated spin relaxation in monolayer $\mathrm{MoS_2}$, Phys. Rev. B **87**, 245421 (2013).
[2] D. Xiao, G.-B. Liu, W. Feng, X. Xu, and W. Yao, Coupled Spin and Valley Physics in Monolayers of $\mathrm{MoS_2}$ and Other Group-VI Dichalcogenides, Phys. Rev. Lett. **108**, 196802 (2012).

[3] X. Liu, G. Zhang, Q.-X. Pei, and Y.-W. Zhang, Phonon thermal conductivity of monolayer MoS_2 sheet and nanoribbons, Appl. Phys. Lett. **103**, 133113 (2013).

[4] Z. Gong, G.-B. Liu, H. Yu, D. Xiao, X. Cui, X. Xu, and W. Yao, Magnetoelectric effects and valley-controlled spin quantum gates in transition metal dichalcogenide bilayers, Nat. Commun. **4**, 2053 (2013).

[5] T. Yokoyama, Controllable valley and spin transport in ferromagnetic silicene junctions, Phys. Rev. B **87**, 241409 (2013).

[6] W.-T. Lu, H.-Y. Tian, H.-M. Liu, Y.-F. Li, and W. Li, Spin- and valley-dependent negative magnetoresistance in a ferromagnetic MoS_2 junction with a quantum well, Phys. Rev. B **98**, 075405 (2018).

[7] X.-J. Qiu, Z.-Z. Cao, J. Hou, and C.-Y. Yang, Controlled giant magnetoresistance and spin–valley transport in an asymmetrical MoS_2 tunnel junction, Appl. Phys. Lett. **117**, 102401 (2020).

[8] J. Wunderlich, B. Kaestner, J. Sinova, and T. Jungwirth, Experimental Observation of the Spin-Hall Effect in a Two-Dimensional Spin-Orbit Coupled Semiconductor System, Phys. Rev. Lett. **94**, 047204 (2005).

[9] Y. K. Kato, R. C. Myers, A. C. Gossard, and D. D. Awschalom, Observation of the spin Hall effect in semiconductors, Science **306**, 1910 (2004).

[10] M. Z. Hasan and C. L. Kane, Colloquium: Topological insulators, Rev. Mod. Phys. **82**, 3045 (2010).

[11] X.-L. Qi and S.-C. Zhang, Topological insulators and superconductors, Rev. Mod. Phys. **83**, 1057 (2011).

[12] Y.-J. Lin, K. Jiménez-García, and I. B. Spielman, Spin–orbit-coupled Bose–Einstein condensates, Nature **471**, 83 (2011).

[13] X.-J. Hao, R.-Y. Yuan, T. Ji, and Y. Guo, Switch effect for spin-valley electrons in monolayer WSe_2 structures subjected to optical field and Fermi velocity barrier, J. Appl. Phys. **128**, 154303 (2020).

[14] X. Zhai, R. Wen, X. Zhou, W. Chen, W. Yan, L.-Y. Gong, Y. Pu, and X. Li, Valley-Mediated and Electrically Switched Bipolar-Unipolar Transition of the Spin-Diode Effect in Heavy Group-IV Monolayers, Phys. Rev. Appl. **11**, 064047 (2019).

[15] Y. Hajati, M. Alipourzadeh, and I. Makhfudz, Spin-valley dependent Klein tunneling and perfect spin- and valley-polarized transport in a magnetic WSe_2 superlattice, Phys. Rev. B **104**, 205402 (2021).

[16] M. Alipourzadeh, Y. Hajati, and I. Makhfudz, Photo- and exchange-field controlled line-type resonant peaks and enhanced spin and valley polarizations in a magnetic WSe_2 junction, J. Phys. D: Appl. Phys. **55**, 165301 (2022).

[17] D.-N. Liu and Y. Guo, Optoelectronic superlattices based on 2D transition metal dichalcogenides, Appl. Phys. Lett. **118**, 123101 (2021).

[18] D. Zambrano, P. Orellana, L. Rosales, and A. Latgé, Spin and Valley Filter Based on Two-Dimensional WSe_2 Heterostructures, Phys. Rev. Appl. **15**, 034069 (2021).

[19] D. Liu, B. Liu, R. Yuan, J. Zheng, and Y. Guo, Valley filter and valley valve based on WSe_2 double-barrier junctions modulated by polarized light, Phys. Rev. B **103**, 245432 (2021).

[20] A. M. Jones, H. Yu, J. S. Ross, P. Klement, N. J. Ghimire, J. Yan, D. G. Mandrus, W. Yao, and X. Xu, Spin–layer locking effects in optical orientation of exciton spin in bilayer WSe_2, Nat. Phys. **10**, 130 (2014).

[21] M. Zubair, M. Tahir, P. Vasilopoulos, and K. Sabeeh, Quantum magnetotransport in bilayer MoS_2: Influence of perpendicular electric field, Phys. Rev. B **96**, 045405 (2017).

[22] M. Tahir, P. Krstajić, and P. Vasilopoulos, Electrically controlled dc and ac transport in bilayer WSe_2, Phys. Rev. B **98**, 075429 (2018).

[23] V. Vargiamidis, P. Vasilopoulos, M. Tahir, and N. Neophytou, Berry curvature, orbital magnetization, and Nernst effect in biased bilayer WSe_2, Phys. Rev. B **102**, 235426 (2020).

[24] C. Jiang, F. Liu, J. Cuadra, Z. Huang, K. Li, A. Rasmita, A. Srivastava, Z. Liu, and W.-B. Gao, Zeeman splitting via spin-valley-layer coupling in bilayer $MoTe_2$, Nat. Commun. **8**, 802 (2017).

[25] S. Wu, J. S. Ross, G.-B. Liu, G. Aivazian, A. Jones, Z. Fei, W. Zhu, D. Xiao, W. Yao, and D. Cobden, *et al.*, Electrical tuning of valley magnetic moment through symmetry control in bilayer MoS_2, Nat. Phys. **9**, 149 (2013).

[26] M. Zubair, M. Tahir, and P. Vasilopoulos, Magneto-optical properties of bilayer transition metal dichalcogenides, Phys. Rev. B **98**, 155402 (2018).

[27] B. Van Duppen and F. Peeters, Four-band tunneling in bilayer graphene, Phys. Rev. B **87**, 205427 (2013).

[28] H. Khani and S. P. Pishekloo, Gate-controlled spin–valley–layer locking in bilayer transition-metal dichalcogenides, Nanoscale **12**, 22281 (2020).

[29] H. Li, J. Shao, D. Yao, and G. Yang, Gate-voltage-controlled spin and valley polarization transport in a normal/ferromagnetic/normal MoS_2 junction, ACS Appl. Mater. Interfaces **6**, 1759 (2014).

[30] X. Qiu, Q. Lv, and Z. Cao, Optical, electric and magnetic controlled ballistic conductance in monolayer WSe_2: The perfect valley and spin polarizations, J. Phys. D: Appl. Phys. **50**, 455106 (2017).

[31] M. Büttiker, Four-Terminal Phase-Coherent Conductance, Phys. Rev. Lett. **57**, 1761 (1986).

[32] X.-J. Hao, R.-Y. Yuan, J.-J. Jin, and Y. Guo, Influence of the velocity barrier on the massive Dirac electron transport in a monolayer MoS_2 quantum structure, Front. Phys. **15**, 33603 (2020).

[33] A. Kormányos, G. Burkard, M. Gmitra, J. Fabian, V. Zólyomi, N. D. Drummond, and V. Fal'ko, $\mathbf{k}\cdot\mathbf{p}$ theory for two-dimensional transition metal dichalcogenide semiconductors, 2D Mater. **2**, 022001 (2015).

[34] J. A. Wilson and A. Yoffe, The transition metal dichalcogenides discussion and interpretation of the observed optical, electrical and structural properties, Adv. Phys. **18**, 193 (1969).

[35] A. Eftekhari, Tungsten dichalcogenides (WS_2, WSe_2, and WTe_2): Materials chemistry and applications, J. Mater. Chem. A **5**, 18299 (2017).

[36] J. Kopaczek, S. Zelewski, K. Yumigeta, R. Sailus, S. Tongay, and R. Kudrawiec, Temperature dependence of the indirect gap and the direct optical transitions at the high-symmetry point of the Brillouin zone and band nesting in

MoS_2, $MoSe_2$, $MoTe_2$, WS_2, and WSe_2 crystals, J. Phys. Chem. C **126**, 5665 (2022).

[37] B. Scharf, G. Xu, A. Matos-Abiague, and I. Žutić, Magnetic Proximity Effects in Transition-Metal Dichalcogenides: Converting Excitons, Phys. Rev. Lett. **119**, 127403 (2017).

[38] M. Tahir, P. M. Krstajić, and P. Vasilopoulos, Magnetic and electric control of spin- and valley-polarized transport across tunnel junctions on monolayer WSe_2, Phys. Rev. B **95**, 235402 (2017).

[39] Q. Yang, R. Yuan, and Y. Guo, Valley switch effect based on monolayer WSe_2 modulated by circularly polarized light and valley Zeeman field, J. Phys. D: Appl. Phys. **52**, 335301 (2019).

[40] Y. Hajati, M. Alipourzadeh, and I. Makhfudz, Spin- and valley-polarized transport and magnetoresistance in asymmetric ferromagnetic WSe_2 tunnel junctions, Phys. Rev. B **103**, 245435 (2021).

[41] P. Lautenschlager, P. Allen, and M. Cardona, Temperature dependence of band gaps in Si and Ge, Phys. Rev. B **31**, 2163 (1985).

[42] A. Srivastava, M. Sidler, A. V. Allain, D. S. Lembke, A. Kis, and A. Imamoğlu, Valley Zeeman effect in elementary optical excitations of monolayer WSe_2, Nat. Phys. **11**, 141 (2015).

[43] J. Lee, K. F. Mak, and J. Shan, Electrical control of the valley Hall effect in bilayer MoS_2 transistors, Nat. Nanotechnol. **11**, 421 (2016).

[44] C. Zhao, T. Norden, P. Zhang, P. Zhao, Y. Cheng, F. Sun, J. P. Parry, P. Taheri, J. Wang, and Y. Yang, *et al.*, Enhanced valley splitting in monolayer WSe_2 due to magnetic exchange field, Nat. Nanotechnol. **12**, 757 (2017).

[45] L. Xu, M. Yang, L. Shen, J. Zhou, T. Zhu, and Y. P. Feng, Large valley splitting in monolayer WS_2 by proximity coupling to an insulating antiferromagnetic substrate, Phys. Rev. B **97**, 041405 (2018).

[46] Y.-F. Wu, H.-D. Song, L. Zhang, X. Yang, Z. Ren, D. Liu, H.-C. Wu, J. Wu, J.-G. Li, and Z. Jia, *et al.*, Magnetic proximity effect in graphene coupled to a $BiFeO_3$ nanoplate, Phys. Rev. B **95**, 195426 (2017).

[47] Z. Qiao, W. Ren, H. Chen, L. Bellaiche, Z. Zhang, A. MacDonald, and Q. Niu, Quantum Anomalous Hall Effect in Graphene Proximity Coupled to an Antiferromagnetic Insulator, Phys. Rev. Lett. **112**, 116404 (2014).

[48] K. L. Seyler, D. Zhong, B. Huang, X. Linpeng, N. P. Wilson, T. Taniguchi, K. Watanabe, W. Yao, D. Xiao, and M. A. McGuire, *et al.*, Valley manipulation by optically tuning the magnetic proximity effect in WSe_2/CrI_3 heterostructures, Nano Lett. **18**, 3823 (2018).

[49] K. Zollner, P. E. F. Junior, and J. Fabian, Proximity exchange effects in $MoSe_2$ and WSe_2 heterostructures with CrI_3: Twist angle, layer, and gate dependence, Phys. Rev. B **100**, 085128 (2019).

[50] C. Ke, Y. Wu, W. Yang, Z. Wu, C. Zhang, X. Li, and J. Kang, Large and controllable spin-valley splitting in two-dimensional WS_2/*h*-VN heterostructure, Phys. Rev. B **100**, 195435 (2019).

[51] J. Qi, X. Li, Q. Niu, and J. Feng, Giant and tunable valley degeneracy splitting in $MoTe_2$, Phys. Rev. B **92**, 121403 (2015).

[52] Q. Zhang, S. A. Yang, W. Mi, Y. Cheng, and U. Schwingenschlögl, Large spin-valley polarization in monolayer $MoTe_2$ on top of EuO (111), Adv. Mater. **28**, 959 (2016).

[53] A. Hallal, F. Ibrahim, H. Yang, S. Roche, and M. Chshiev, Tailoring magnetic insulator proximity effects in graphene: First-principles calculations, 2D Mater. **4**, 025074 (2017).

[54] M. Yankowitz, D. McKenzie, and B. J. LeRoy, Local Spectroscopic Characterization of Spin and Layer Polarization in WSe_2, Phys. Rev. Lett. **115**, 136803 (2015).

[55] K. Tran, A. Singh, J. Seifert, Y. Wang, K. Hao, J.-K. Huang, L.-J. Li, T. Taniguchi, K. Watanabe, and X. Li, Disorder-dependent valley properties in monolayer WSe_2, Phys. Rev. B **96**, 041302 (2017).